Journal of Applied Fluid Mechanics, Vol. 16, No. 9, pp. 1865-1876, 2023.
Available online at www.jafmonline.net, ISSN 1735-3572, EISSN 1735-3645.
https://doi.org/10.47176/jafm.16.09.1749

Assessment of Total Pressure and Swirl Distortions in a Busemann Inlet at Mach 6

Y. Li†[1], Z. Wu[1], S. Wu[1], S. Hu[1], and F. Wei[2]

[1]*School of Aircraft Engineering, Nanchang Hangkong University, No. 696, Fenghenan Road, Nanchang, 100190, Jiangxi, P.R. China*
[2]*Science and Technology on Scramjet Laboratory，China Aerodynamics Research and Development Center, MianYang, 621000, China，Aerospace Technology Institute*

†*Corresponding Author Email: yiqingxmu@163.com*

ABSTRACT

Flow distortions in high-speed inlet systems are complex, and high-performance air-breathing propulsion systems. In this paper, large eddy simulations are performed to study the total pressure and swirl distortions in a Busemann inlet at freestream Mach number 6. The on-design flow condition with both the Attack Angle and Sideslip Angle equal to zero and two off-design conditions (Attack Angle = 6 deg, Sideslip Angle = 0 deg and Attack Angle = 6 deg, Sideslip Angle = 6 deg) are considered to explore the flow characteristics inside the inlet duct as well as the distortions at the inlet exit plane. It is found that under the on-design flow condition, the shock structures and boundary layer development are nearly axisymmetric about the inlet axis. The captured freestream is compressed smoothly through inlet duct. The total pressure loss is limited primarily to within the boundary layer region, and nearly no swirling flow is introduced during the flow compression process. Under the off-design flow conditions, the shock structures inside the inlet duct become non-axisymmetric, and localized strong shock–boundary layer interactions occur. In the case of the off-design flow condition with Attack Angle = 6 deg, Sideslip Angle = 0 deg, a large flow separation zone appears owing to the incidence of a strong curved shock on the wall surface at the leeward side in the inlet duct, and the low-kinetic-energy flow contained in this flow separation zone leads to an obvious total-pressure reduction at the exit plane of inlet. Meanwhile, a large-scale swirling flow is formed at the exit plane of inlet owing to the appearance of a nonuniform transverse pressure gradient. Under the off-design conditions, a pair of vortex is observed at the exit plane of inlet. The shock wave–boundary layer interactions under the off-design conditions are stronger than those under the on-design condition, which results in more intense total pressure and swirl distortions. The averages of the fluctuating distortions are more evident than the temporal-averaged total-pressure and swirl distortions. These results show that turbulent flow fluctuations are important in determining the overall distortion level in a Busemann inlet.

Article History

Received January 8, 2023
Revised April 20, 2023
Accepted May 1, 2023
Available online July 1, 2023

Keywords:

Hypersonic inlet
Busemann inlet
Large eddy simulation
Total pressure distortion
Swirl distortion
Shock wave–boundary layer interaction

1. INTRODUCTION

A Busemann inlet is a type of typical hypersonic inlet that compresses a uniform axisymmetric freestream isentropically through conical shockwaves with high compression efficiency and minimum total pressure loss (Mölder & Szpiro, 1966; Flock & Gülhan 2016, Ma et al., 2020; Brahmachary & Ogawa 2021). However, its use of an ideal conical compression surface has limited its wide application in practical hypersonic aircraft design owing to the difficulties of integration with various types of hypersonic airframe, and therefore more practical hypersonic integration design concepts such as lift body/inlet integration and inward turning inlet/waverider forebody integration have become predominant (Ding et al., 2015; Wang et al., 2016; Luo et al., 2022; Ramunno et al., 2022). Wang et al. (2015) employed a design method that integrated an inward-turning inlet and the airframe. Rectangular-to-circular, erose-to-circular, and sector-to-circular shape transition Busemann inlets have been designed for integration with three airframes. Wang et al. (2016) proposed a new design method for integration of a multistage compression osculating cone waverider and a Busemann inlet. Yu et al. (2020) proposed a novel three-

Nomenclature

AoA	attack angle	W	conserved variable vector
Beta	sideslip angle	W_L	solution vector located on left side
CR	area contraction ratio	W_R	solution vector located on right side
C_ω	model coefficient	X	inlet axial length
dS	closed surface	δW	spatial difference
F_{inv}	inviscid flux vector	μ_t	eddy-viscosity coefficient
F_{vis}	viscous flux vector	Ω	control volume
$\bar{S}_{ij}$	strain velocity tensor		

dimensional (3D) inverse method of characteristics (MOC) to design the inlet lip with a generalized 3D shock and found that this method provided a promising solution for the hypersonic internal/external coupling flow. The integrated design of a Busemann inlet with a third-stage compression surface has a greater lift-to-drag ratio, more uniformly compressed flow, and greater total pressure recovery coefficient.

It should be noted that even though the geometrical configurations of practical hypersonic inlets are much more complex than that of a Busemann inlet, the basic flowfields for many new design concepts originated from the ideal Busemann basic flow. In other words, the new integrated inlets inherit both the advantages and disadvantages as well as the fundamental flow features of a Busemann inlet (Ding et al., 2018; Xiong et al., 2019; Musa et al., 2022). Shock wave–boundary layer interaction and a nonuniform transverse pressure distribution are two key influences on the performance of hypersonic inlets (Schulte et al., 2001; Zhang et al., 2014). They can lead to flow separation, total pressure loss, swirl flow, and even unstart of the inlet (Xie et al., 2018; Xu et al., 2022; Zhai et al., 2022). For a Busemann-originated inlet under off-design flow conditions, the mass capture rate and the total pressure recovery coefficient are decreased, and nonuniformities in the pressure and the velocity magnitude at the inlet exit plane are increased. Bachchan & Hillie (2004a, b) found that inlet flow nonuniformities can be caused by off-design shock wave interactions or viscous effects. Inlet flow nonuniformities make it increasingly difficult to stabilize the terminal shock system and, for actual inlet configurations, lead to the occurrence of a variety of unsteady flow phenomena. Flow distortions at the inlet exit plane are inevitable with Busemann-originated hypersonic inlets, and their influence on downstream engine components deserves more attention.

The total pressure and swirl distortions can be transferred through the inlet isolator and exert a great influence on fuel mixing and combustion in scramjet combustors. Malo-Molina et al. (2010) employed 3D numerical simulations to examine the effects of inlet distortion on a generic supersonic combustor with circular cross-section at a flight condition of Mach 6 and at an altitude of about 24.2 km. Their results indicate that the overall combustor performance decreases owing to the complex flow distortion from the inlet. In a supersonic flow, Ombrello et al. (2015) experimentally studied the effects of inflow distortion on ignition within a cavity-based flameholder. They observed that the upstream flow distortion greatly influences the fuel injection mass flow rate and the spark energy needed from the ignitor. McGann et al. (2019) studied the fuel–air distribution and ignition in a scramjet cavity flameholder using nanosecond-gated laser-induced breakdown spectroscopy. They found that upstream flow distortion can greatly influence the cavity shear layer, fuel distribution, and local gas density within the cavity. It should be noted that although the above studies have revealed the important influence of flow distortion on the performance of hypersonic propulsion systems, there is still a lack of adequate information about the types of flow distortion, the flow distortion levels, and the spatial distributions of flow distortion.

Compared with a conventional turbo aeroengine, the engine components in a hypersonic propulsion system are greatly simplified (Heiser et al., 1994). The freestream captured by the inlet undergoes fuel injection, air–fuel mixing, ignition, combustion, and expansion. Flow distortion directly influences all those processes. Flow distortion in conventional turbo aeroengines has been intensively studied over the past few decades (AIR5686 2010; AIR1419C 2017; ARP1420C 2017), but few studies have examined flow distortion quantitatively or presented explicit methods to calibrate the levels of flow distortion in hypersonic inlets. In the present study, the fundamental flow features of a Busemann inlet under on-design and off-design freestream conditions are investigated numerically by large eddy simulation (LES). The inlet total-pressure and swirl distortions of are quantitatively characterized through distortion descriptors. An in-depth analysis is performed on both time-averaged flow data and instantaneous turbulent flow information. The results reveal important features of flow distortion in hypersonic inward compression inlets. The methods adopted here for assessing total pressure distortion and swirl distortion could be used as a reference assessment framework for similar types of hypersonic inlet. Tho results will be helpful for the development of high-performance hypersonic propulsion.

The organization of the remainder of the paper is as follows. Section 2 introduces the numerical methodologies. The Busemann inlet model, computational grid, numerical schemes, and turbulence model are presented. In Sec. 3, both time-averaged flow features and transient flow data for a Busemann inlet operating under on-design and off-design conditions are analyzed. Streamlines and velocity divergence contours are presented to reveal the fundamental flow features of the

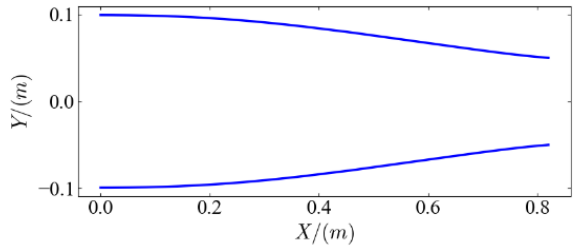

Fig. 1. Busemann inlet profile.

Busemann inlet. In Sec. 4, the total pressure and swirl distortions at the inlet exit plane are quantified through distortion descriptors. Comparisons are made between the time-averaged and instantaneous distortion descriptors. In Sec.5, discussions and conclusions are given.

2. COMPUTATIONAL METHODS

2.1 Busemann Inlet Model and Grid

The Busemann inlet profile is shown in Fig. 1. The profile of the inlet is designed using the MOC at a freestream Mach number of 6.0, with the on-design condition set as an Attack Angle of 0 deg and a Sideslip Angle of 0 deg. The total length of the inlet is 0.82 m. The radii of the axisymmetric inlet entrance and exit planes are 0.0992 m and 0.05 m, respectively. The area contraction ratio (CR), which is given by the ratio of entrance area to exit area, is 3.94. For convenience in the subsequent analysis, the inlet entrance is designated as plane 1 and the exit plane as plane 2.

Figure 2 shows a schematic of the Busemann inlet grid. The computational domain is filled with hexahedral cells. Along the streamwise direction, the grid spacing is uniform. A denser grid spacing is applied near the inlet wall area for better resolution of the boundary layer.

2.2 Numerical Schemes

Numerical simulations are performed by an in-house developed solver. The flowfields of the Busemann inlet with freestream Mach number 6.0 are simulated by LES. The 3D compressible Navier–Stokes equations are discretized using the finite volume method (Geurts et al., 1993). The governing equations is written as (Zhang et al., 2017):

$$\frac{\partial}{\partial t}\int_{\Omega}\mathbf{W}\,\mathrm{d}\Omega+\oint_{\partial\Omega}\left(\mathbf{F}_{\mathrm{inv}}-\mathbf{F}_{\mathrm{vis}}\right)\mathrm{d}S=0, \tag{1}$$

where the control volume Ω is closed by cell surface $\mathrm{d}S$. $\mathbf{W}$ is the conserved variable vector, $\mathbf{F}_{\mathrm{inv}}$ is the inviscid flux vector, and $\mathbf{F}_{\mathrm{vis}}$ is the viscous flux vector. When the inviscid convective fluxes are discretized by Roe's flux-difference splitting scheme, $\mathbf{F}_{\mathrm{inv}}$ can be expressed as

$$\mathbf{F}_{\mathrm{inv}}=\tfrac{1}{2}\left(\mathbf{F}_{R,\mathrm{inv}}+\mathbf{F}_{L,\mathrm{inv}}\right)-\tfrac{1}{2}\Gamma\left|\hat{A}\right|\delta\mathbf{W}. \tag{2}$$

The solution vectors $\mathbf{W}_R$ and $\mathbf{W}_L$ located on the left and right sides of the face are used to calculate $\mathbf{F}_{R,\mathrm{inv}}$ and $\mathbf{F}_{L,\mathrm{inv}}$, and the spatial difference $\delta\mathbf{W}$ is obtained as

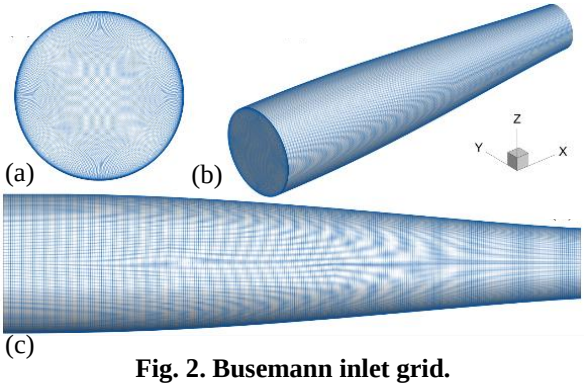

Fig. 2. Busemann inlet grid.

$\mathbf{W}_R-\mathbf{W}_L$. The second-order centered difference scheme is used to discretize the viscous fluxes, and the advanced time method is point implicit.

The turbulence model is based on a wall-adapting local eddy-viscosity (WALE) LES model and the eddy-viscosity coefficient is calculated using the following formula:

$$\mu_t=\rho\Delta_s^2\frac{\left(S_{ij}^dS_{ij}^d\right)^{3/2}}{\left(\bar{S}_{ij}\bar{S}_{ij}\right)^{5/2}+\left(S_{ij}^dS_{ij}^d\right)^{5/4}}. \tag{3}$$

To keep the notation concise, the coordinates in the three directions (X,Y,Z) are denoted by x_i $(i=1,2,3)$ and the velocities (u,v,w) in these three directions are denoted by u_i $(i=1,2,3)$. The relevant parameters in Eq. (3) are calculated as follows:

$$\Delta_s=C_\omega V^{1/3}, \tag{4}$$

$$S_{ij}^d=\tfrac{1}{2}\left(\bar{g}_{ij}^2+\bar{g}_{ji}^2\right)-\tfrac{1}{3}\delta_{ij}\bar{g}_{kk}^2, \tag{5}$$

$$\bar{g}_{ij}=\frac{\partial\bar{u}_i}{\partial\bar{x}_j}, \tag{6}$$

$$\bar{g}_{ij}^2=\bar{g}_{ik}\bar{g}_{kj}, \tag{7}$$

where $\bar{S}_{ij}$ is the strain velocity tensor, which can be obtained from by resolved velocity field:

$$\bar{S}_{ij}=\frac{1}{2}\left(\frac{\partial\bar{u}_i}{\partial\bar{x}_j}+\frac{\partial\bar{u}_j}{\partial\bar{x}_i}\right). \tag{8}$$

In the WALE model, the model coefficient is

$$C_\omega=0.325. \tag{9}$$

For inlet wall surface, the adiabatic wall-boundary is utilized according to the formula:

$$q_s=-\kappa\frac{\mathrm{d}\bar{T}}{\mathrm{d}\bar{x}_{\text{wall-normal}}}=0. \tag{10}$$

2.3 Grid Convergence Study

First of all, grid convergence is verified through three sets of computational grids. The configurations of the computational grids are shown in Table 1. The first cell height near the wall decreases from 0.05 mm to 0.01 mm

Table 1 Grid Parameters

Grid	Cell No.	Wall first cell height (mm)	Cell wall normal height ratio
G1	10299968	0.05	1.05
G2	20046724	0.04	1.05
G3	30176542	0.01	1.05

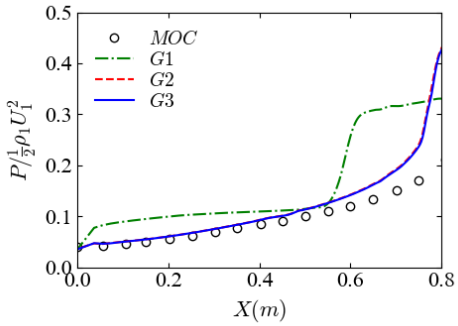

Fig. 3. Normalized wall static pressure distributions.

for grids G1 to G3 while the cell wall normal height ratio is kept constant. The total number of computational cells increases from approximately 10 million to 30 million for grids G1 to G3.

The on-design flow parameters are used to perform simulations. The freestream Mach number is 6.0, and the static pressure and static temperature are 2549 Pa and 221 K, respectively. Figure 3 shows the normalized wall static pressure distributions obtained with the three grids. It can be seen that the pressure distribution obtained using grid G1 deviates from the MOC results. This suggests that grid G1 cannot sufficiently resolve the flow parameters within the boundary layer, leading to a strong shock at X = 0.55 m. The pressure distributions obtained using grids G2 and G3 overlap with each other and show much better agreement with the MOC data than the distribution obtained using the G1 grid. The deviations of the pressure distributions obtained using grids G2 and G3 from the MOC data at X > 0.5 m are understandable, since the MOC data are based on inviscid calculations and the boundary layer development is not accounted for in the MOC. To better resolve small-scale turbulent structures in LES, grid G3 is used for the subsequent simulations.

2.4 Distortion Descriptors

According to the inlet distortion standards (AIR5686, 2010; AIR1419C, 2017) published by the Society of Automotive Engineers (SAE), the inlet total pressure and swirl distortions should be evaluated through distortion descriptors. For the inlet total pressure distortion, the distortion extent *EXT*, the circumferential distortion intensity *CDI*, the radial distortion intensity *RDI*, and the multi-per revolution *MPR* are adopted as distortion descriptors (AIR1419C, 2017). For inlet swirl distortion, the swirl intensity *SI*, swirl direction *SD*, and swirl pairs *SP* are adopted as distortion descriptors (AIR5686, 2010). The detailed mathematical expressions for these descriptors can be found in the SAE standards documents.

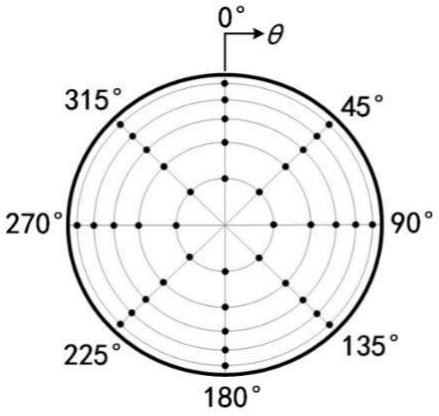

Fig. 4. The 40 probe measurement rake locations (ARP1420C).

It should be noted that the total pressure and swirl distortion descriptors were originally developed to assess inlet distortion for turbo engines. Nevertheless, these distortion descriptors fundamentally reflect the spatially nonuniform distribution of total pressure and swirl characteristics for a circular inlet exit plane. Thus, it is reasonable to use the total pressure and swirl distortion descriptors developed by the SAE to evaluate distortion in the case of a Busemann inlet under hypersonic freestream conditions. To evaluate the inlet total pressure and swirl distortions, raw total pressure and velocity data are calibrated at the inlet exit plane. For an inlet with a circular exit plane, typically 40 probe measurement rakes are installed in wind tunnel tests to record total pressure data and velocity data. Figure 4 shows 40 probe measurement rake locations for the inlet exit plane (ARP1420C, 2010). The black dots represent pressure transducer or velocity sensor locations for data measurement. There are eight rakes, and five measurement locations are fixed on each rake. To increase the spatial resolution, the number of rakes in the probing simulation data was increased from 8 to 360, and thus the total number of raw total pressure or velocity data for each case is 5×360.

3. INLET FLOW CHARACTERISTICS

Three sets of freestream conditions are used for LES. The freestream Mach number, static pressure, and static temperature are identical to the parameters used in Sec. 2.3. The Attack Angle = 0 deg, Sideslip Angle = 0 deg condition, which is denoted as C1, is the baseline for the on-design condition, while Attack Angle = 6 deg, Sideslip Angle = 0 deg and Attack Angle = 6 deg, Sideslip Angle = 6 deg are off-design conditions in comparison with on-design condition, which are denoted as C2 and C3, respectively. Through LES, a large amount of transient flow data is obtained. Both the time-averaged and transient flow characteristics of the Busemann inlet are analyzed in this section.

3.1 Flow Analysis Through Time-Averaged Statistics

Time average operation is performed on flow data by averaging 500 transient data with a temporal gap between two transient flow data of 1×10^{-5} s. Figure 5 shows the

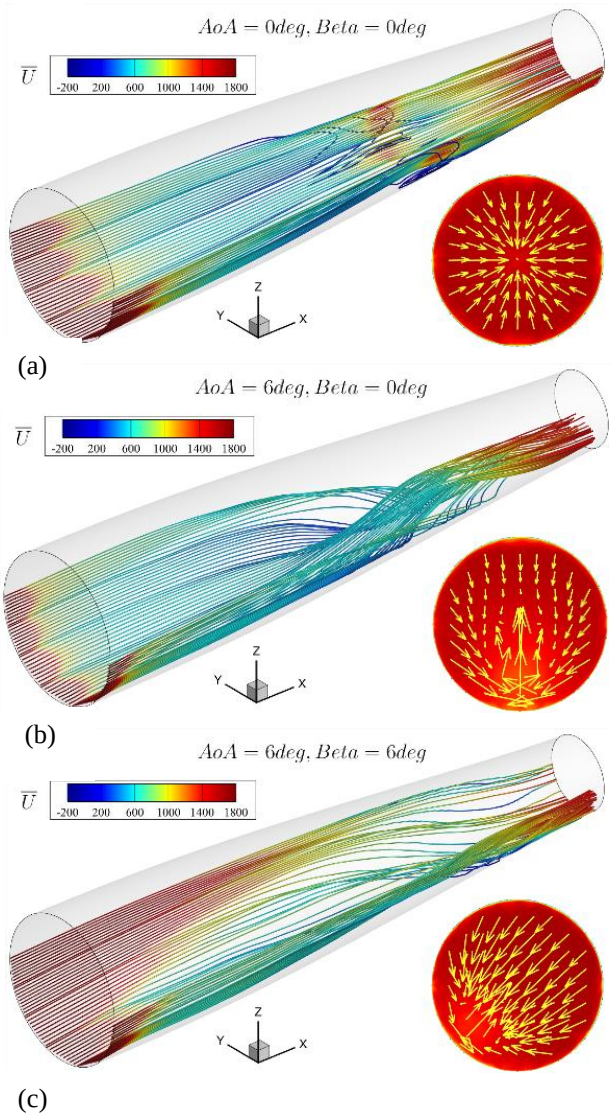

Fig. 5. Busemann inlet streamlines and velocity vectors at exit plane.

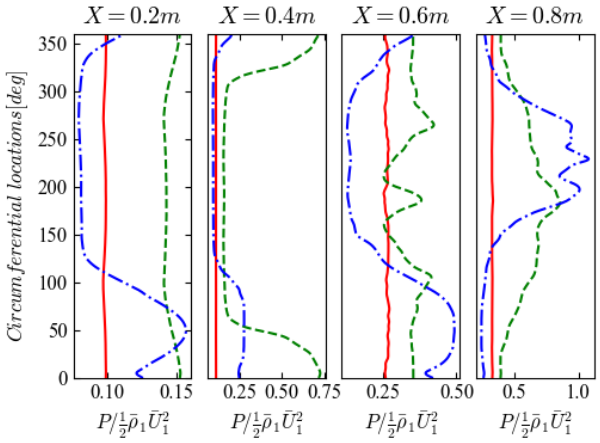

Fig. 6. Busemann inlet time-averaged pressure distributions along the circumferential direction near the wall in different streamwise sections.

streamlines and velocity vectors at the Busemann inlet exit-plane. The streamlines and velocity vectors are generated using the time-averaged velocities in three flow directions. The streamlines are colored by the time-averaged streamwise velocity *U*. As shown in Fig. 5(a), for the on-design condition, Attack Angle = 0 deg, Sideslip Angle = 0 deg, the streamlines near the wall surface are relatively straight from the inlet entrance plane to the exit plane. Shock wave–boundary layer interaction leads to slight flow separation near the wall approximating the middle streamwise plane of the inlet duct. The blue parts of the streamlines near the separation region indicate that the time-averaged streamwise velocity *U* is negative. At the exit plane, the velocity vectors converge to the geometrical center of the plane owing to the area contraction through Busemann inlet convergence duct. For Attack Angle = 6 deg, Sideslip Angle = 0 deg, as shown in Fig. 5(b), the freestream angle of attack leads to swirling flow in the inlet duct, and the streamlines near the two side walls begin to gather around the bottom wall when flowing downstream. At the inlet exit plane, it can be observed that the velocity vectors near the two sidewalls converge to the bottom wall and meanwhile the velocity vectors near the bottom wall begin to flow vertically to the geometrical center of inlet cross-section plane. The vector length represents the magnitude of the velocity. It is found that the magnitude of the velocity at the two sidewalls is much larger than that in other regions. This suggests that the flow accelerates when turning toward the bottom of the center of the exit plane. At Attack Angle = 6 deg, Sideslip Angle = 6 deg, as shown in Fig. 5(c), swirling flow is also observed in the inlet duct as well as at the exit plane. Owing to the combined effects of angle of attack as well as angle of sideslip, the streamlines in the inlet duct have an overall 45 deg incline. At the Busemann inlet exit plane, the velocity vectors converge at the bottom wall at the 225 deg location. The lengths of the velocity vectors indicate that the magnitude of the velocity in the 0 deg to 90 deg fan sector is larger. The streamlines and velocity vectors at the exit plane of Busemann inlet for the three freestream conditions suggest that the freestream angle of attack and angle of sideslip will lead to swirling flow in the Busemann inlet.

To analyze the possible reason for swirl generation within the inlet, the time-averaged pressure near the wall at different inlet axial sections (X = 0.2 m, 0.4 m, 0.6 m, and 0.8m) is extracted as shown in Fig. 6. The data probes are located 1 mm above the wall in the wall-normal direction, and the data are displayed along the circumferential direction from 0 deg to 360 deg. The pressure is normalized by the time-averaged dynamic pressure head at the inlet entrance plane. The red solid lines, green dashed lines, and blue dash-dotted lines are the results for conditions C1, C2, and C3, respectively. It can be seen that for C1 (Attack Angle = 0 deg, Sideslip Angle = 0 deg), static pressure distributions at different inlet axial sections are nearly equal along the circumferential direction (red solid lines). In other words, the transverse pressure gradient for C1 is nearly zero, and thus the streamlines shown in Fig. 5(a) are mostly straight along the inlet internal duct. For C2 (Attack Angle = 6 deg, Sideslip Angle = 0 deg) and C3 (Attack Angle = 6 deg, Sideslip Angle = 6 deg), there are high-pressure and low-pressure regions in the pressure distribution along the

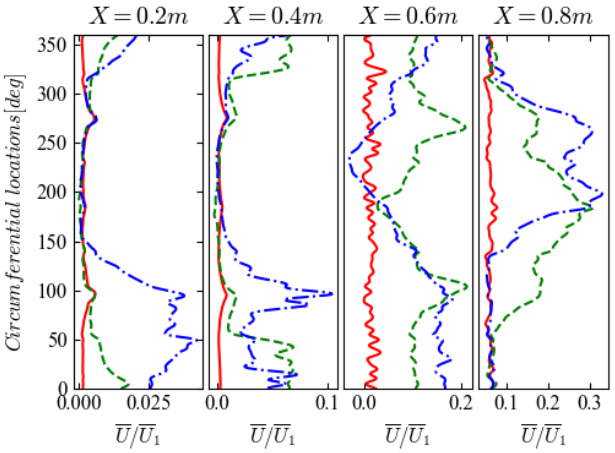

Fig. 7. Busemann inlet time-averaged velocity distributions along the circumferential direction near the wall in different streamwise sections.

circumferential direction. For C2 (green dashed lines), the high-pressure region gradually moves from the top wall to the bottom wall (0 deg to 180 deg) with increasing X location. The development of a local high-pressure region near the wall along the axial sections for C2 indicates that a swirl is formed, with a driving high pressure moving from the top wall at the entrance of the inlet to the bottom wall at the inlet exit plane. Swirl pairs are finally formed at the exit plane of Busemann inlet, as shown in Fig. 5(b). For C3 (blue dash-dotted lines), a similar pressure distribution with a 45 deg circumferential location shift is also observed. The time-averaged normalized streamwise velocity near the wall at different streamwise sections are presented in Fig. 7, where the red solid lines, green dashed lines, and blue dash-dotted lines again show the results for conditions C1, C2, and C3, respectively. It can be seen that for C1, the streamwise velocity distributions at different axial sections are nearly equal along the circumferential direction. The streamwise velocity exhibits a similar distribution to that of the pressure along the circumferential direction for different axial sections. A large streamwise velocity gradient is formed where the pressure gradient is significant. The above observations suggest that the introduction of free stream angle of attack and angle of sideslip result in the formation of a transverse pressure gradient inside the inlet duct. The transverse pressure gradient further drives the captured air to flow transversely on moving downstream. The swirl pairs are finally generated at the exit plane of Busemann inlet under off-design conditions.

The time-averaged aerodynamic performances of the Busemann inlet for the three freestream conditions are shown in Table 2, where $\langle\cdot\rangle$ denotes the spatial–temporal average. As shown in the table, the values of the total pressure recovery coefficient $\langle P_2^*\rangle/\langle P_1^*\rangle$ for conditions C2 and C3 are smaller than the value for C1. This suggests that increases in the angle of attack as well as angle of sideslip lead to stronger shock wave–boundary layer interactions in the inlet duct and consequently result in larger total pressure losses. Among the three conditions, both the static pressure ratio $\langle P_2\rangle/\langle P_1\rangle$ and the static temperature ratio $\langle T_2\rangle/\langle T_1\rangle$ are largest for C2 (Attack

Table 2 Inlet time-averaged aerodynamic performances

Condition	C1	C2	C3
$\langle P_2^*\rangle/\langle P_1^*\rangle$	0.61	0.21	0.50
$\langle P_2\rangle/\langle P_1\rangle$	10.54	12.99	12.04
$\langle T_2\rangle/\langle T_1\rangle$	2.39	3.95	3.02
$\langle Mach_2\rangle$	3.55	2.37	3.18

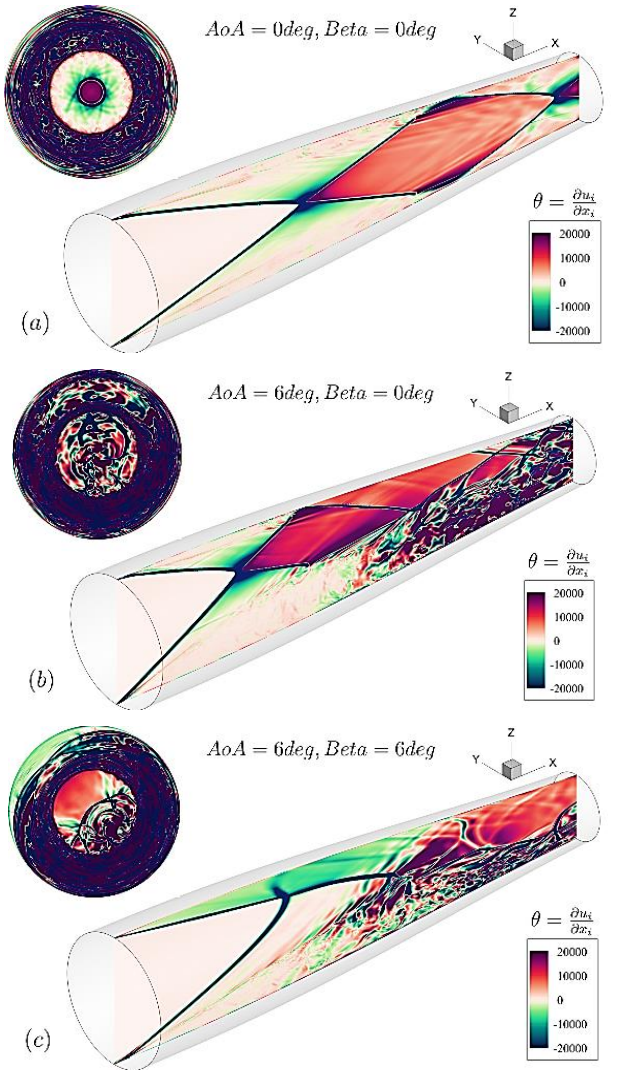

Fig. 8. Contours of instantaneous velocity divergence at inlet central *X*–*Z* plane and inlet exit plane.

Angle = 6 deg, Sideslip Angle = 0 deg). This implies that under off-design conditions in which the angle of attack with respect to the freestream is nonzero but the angle of sideslip is zero, the shock is stronger than when both the angle of attack and angle of sideslip are nonzero. The stronger shock wave–boundary layer interaction leads to a greater total pressure loss and smaller Mach number at the exit plane of Busemann inlet.

3.2 Instantaneous Flow Features

To better visualize the turbulent structures, especially the shock wave structures, in the Busemann inlet, Fig. 8 shows

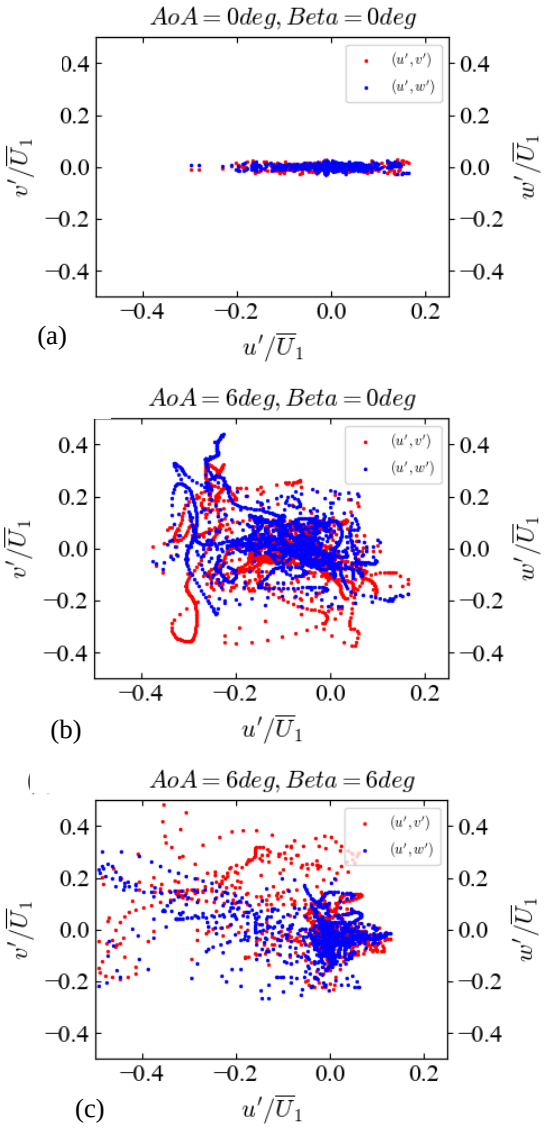

Fig. 9. Scatter plots of fluctuating velocities from the five probe rings.

the contours of instantaneous velocity divergence at the inlet central *X*–*Z* plane and the exit plane of Busemann inlet. The velocity divergence is calculated as $\partial u_i/\partial x_i$. The thin dark lines corresponding to highly compressed flow represent the shock inside the inlet duct. At the conditions of Attack Angle = 0 deg, Sideslip Angle = 0 deg, as shown in Fig. 8(a), the conical shock converges in the center of the inlet duct and is reflected on the inlet wall downstream. The shock structures are axisymmetric throughout the inlet flow path. Small-scale turbulent structures are generated by the shock wave–boundary layer interaction area near the inlet wall. For Attack Angle = 6 deg, Sideslip Angle = 0 deg, as shown in Fig. 8(b), it can be seen that many high-compression and high-expansion structures of different scales are generated inside the inlet duct downstream of the first conical shock. The turbulent structures become dominant inside the inlet internal duct. For Attack Angle = 6 deg, Sideslip Angle = 6 deg, as presented in Fig. 8(c), the incident shock wave becomes more skewed compared with the other two cases. Inside the inlet duct near the bottom wall, a large number of turbulent compression and expansion structures are also observed. At the inlet exit plane under off-design conditions, a large portion of the area is filled with turbulent shock waves and turbulent structures of different scales. This suggests that the flow parameter distributions at the inlet exit plane are largely determined by shock wave–boundary layer interactions upstream inside the inlet duct.

Figure 9 shows scatter plots of the fluctuating velocities from the five probe rings at the exit plane of Busemann inlet for the three inflow conditions. For Attack Angle = 0 deg, Sideslip Angle = 0 deg, as shown in Fig. 9(a), the normalized fluctuating velocity u'varies between −0.3 and 0.2, while the fluctuating velocities v' and w' are relatively small. For Attack Angle = 6 deg, Sideslip Angle = 0 deg, as presented in Fig. 9(b), the three fluctuating velocities have similar magnitudes varying between −0.4 and 0.4. For Attack Angle = 6 deg, Sideslip Angle = 6 deg, as shown in Fig. 9(c), a large portion of the scatter data are found in the region where negative u' predominates. These results suggest that a nonzero angle of attack for the inflow exerts a strong effect in inducing negative u', while nonzero values for both the angle of attack as well as the angle of sideslip have a strong effect in inducing positive v' and w'.

4. BUSEMANN INLET DISTORTIONS

4.1 Inlet Total Pressure Distortion

Figure 10 shows contours of instantaneous total pressure and time-averaged total pressure at the exit plane of Busemann inlet. Turbulent structures near the inlet boundary layer are observed in the instantaneous total pressure contours in Figs. 10(a), 10(c), and 10(e). For the condition of Attack Angle = 0 deg, Sideslip Angle = 0 deg, there are regions of low total pressure located primarily in the turbulent boundary layer near the wall. For the condition of Attack Angle = 6 deg, Sideslip Angle = 0 deg, owing to the strong shock wave–turbulence interaction upstream of the inlet exit plane, most of that plane is filled with low-total-pressure flow. For the condition of Attack Angle = 6 deg, Sideslip Angle = 6 deg, an evident low-total-pressure region is located at 225 deg near Busemann inlet wall. The formation of this low-total-pressure region is due to the accumulation of upstream boundary layer transported by swirling flow. For comparison, the time-averaged total pressure contours at the inlet exit planes are shown in Figs. 10(b), 10(d), and 10(f). It can be seen that for the condition of Attack Angle = 0 deg, Sideslip Angle = 0 deg, the low-total-pressure region is located in the near-wall region. The pattern of the distribution of low total pressure is similar to that of the transient total pressure distribution. For the conditions of Attack Angle = 6 deg, Sideslip Angle = 0 deg and Attack Angle = 6 deg, Sideslip Angle = 6 deg, there are distinct low-total-pressure regions at the exit plane of Busemann inlet. It can be seen that the low-total-pressure region for the condition of Attack Angle = 6 deg, Sideslip Angle = 0 deg is much larger than that for the condition of Attack Angle = 6 deg, Sideslip Angle = 6 deg. This suggests that strong shock wave–boundary layer interaction due to the nonzero angle of attack of the inflow results in critical total pressure

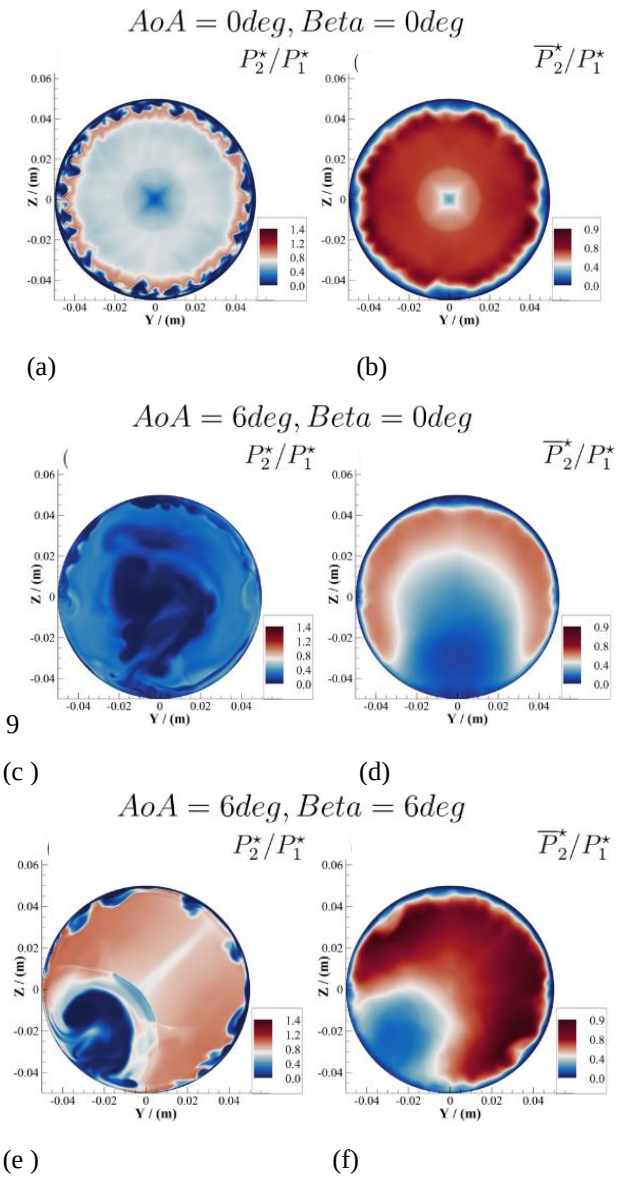

(a) (b) (c) (d) (e) (f)

Fig. 10. Contours of instantaneous and time-averaged normalized total pressure at the exit plane of Busemann inlet.

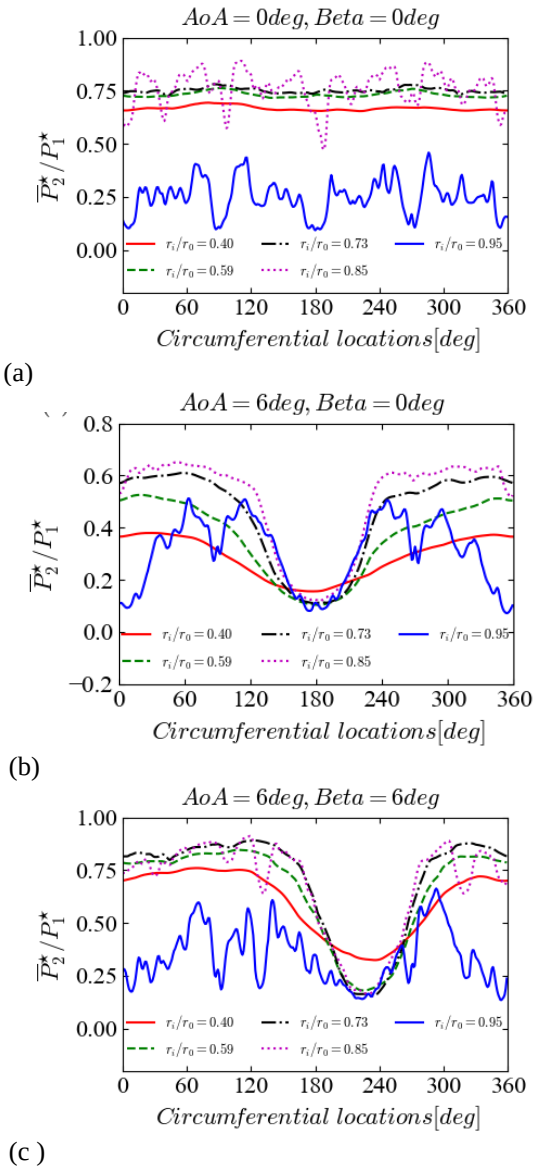

(a) (b) (c)

Fig. 11. Time-averaged total pressure distributions at circumferential locations on five rings.

losses in the inlet duct and leads to the evident low-total-pressure region at the inlet exit plane.

Figure 11 shows the time-averaged total pressure distributions at circumferential locations along five rings. Here, r_i is the radius of each ring and r_0 is the radius of the exit plane of Busemann inlet. For the condition of Attack Angle = 0 deg, Sideslip Angle = 0 deg, the pressure distributions exhibit fluctuating behaviors in the outer rings (r_i/r_0 = 0.85 and 0.95). This is due to the turbulent nature of the boundary layer flow near the wall. In the inner rings (r_i/r_0 = 0.40, 0.59, and 0.73), the total pressure distributions exhibit quasi-steady values for all the circumferential locations. For the condition of Attack Angle = 6 deg, Sideslip Angle = 0 deg, an evident low-pressure region appears near the circumferential location of 180 deg for all five rings. This distribution is consistent with what can be seen in Fig. 10(d), where a low-total-pressure region occupies a large part of the exit plane of Busemann inlet. Similarly, for the condition of Attack Angle = 6 deg, Sideslip Angle = 6 deg, a low-total-pressure region exists near the circumferential location of 235 deg. In the outer ring (r_i/r_0 = 0.95), the total pressure is much lower than those in the other rings.

The inlet distortion descriptors are calculated using two methods. In the first method, the time-averaged values (e.g., time-averaged total pressure and time-averaged velocities) are used as inputs to obtain the distortion descriptors. In the second method, the instantaneous values of the total pressure and the velocities are used directly to calculate the transient distortion descriptors, and an arithmetical average of these transient descriptors is then taken. In the first method, the time-averaged inlet distortion levels are evaluated, whereas the second method takes account of the averaged influence of transient distortion behavior. The total pressure distortion descriptors are presented in Fig. 12. The four distortion descriptors in Figs. 12(a)–12(d) are calculated using the time-averaged total pressure value $\overline{P_2^*}$, while those in Figs.

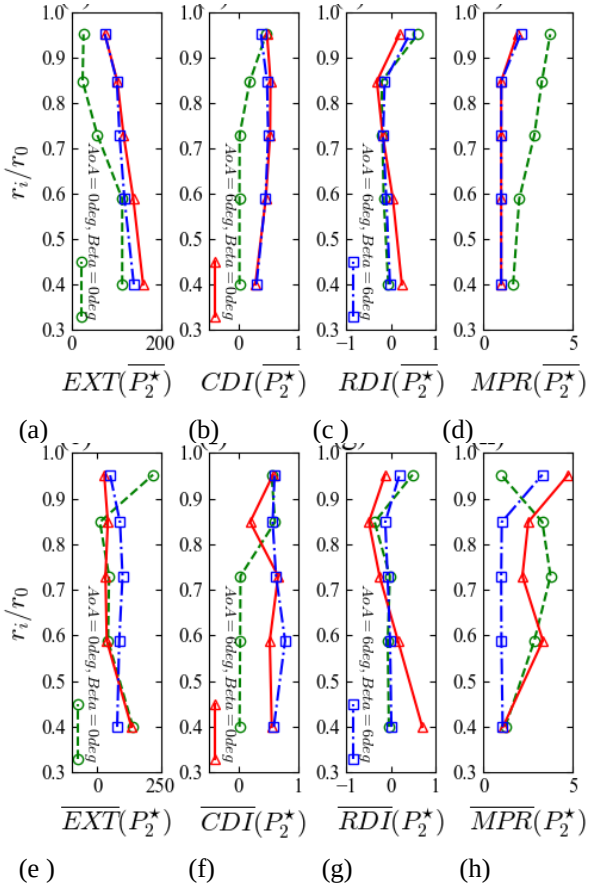

Fig. 12. Total pressure distortion descriptors.

12(e)–12(h) are averaged values based on the fluctuating total pressure P_2^*. It can be seen that the time-averaged distortion extent *EXT* and the circumferential distortion intensity *CDI* for the two off-design conditions are larger than those for the on-design condition on different rings. This is due to the presence of a low total pressure region at the exit plane of Busemann inlet for the off-design inflow conditions. On the inner rings (r_i/r_0 = 0.40, 0.59, and 0.73), the radial distortion intensity *RDI* for Attack Angle = 6 deg, Sideslip Angle = 6 deg is larger than those for the other two conditions. This is due to the large low total pressure region shown in Fig. 10(d). The values of the averaged total pressure distortion descriptors shown in Figs. 12(e)–12(h) are larger than the values of the descriptors based on the time-averaged inputs. These results indicated that the averaged fluctuating distortion levels are larger than the distortion levels calculated from the time-averaged inputs. The fluctuating total pressure distortions resulting from the highly turbulent structures need to be seriously considered in designing of hypersonic aircraft.

4.2 Inlet Swirl Distortion

To calculate the swirl distortion descriptors for a Busemann inlet, the swirl angle α is required. This angle is given by $\alpha = \tan^{-1}(U_\theta/U_x)$, where the circumferential and axial velocities U_θ and U_x, respectively, can be computed from the three velocities u, v, w in Cartesian coordinates (AIR5686 2010). Figure 13 shows contours of the instantaneous swirl and time-averaged swirl angles at the inlet exit plane. It can be

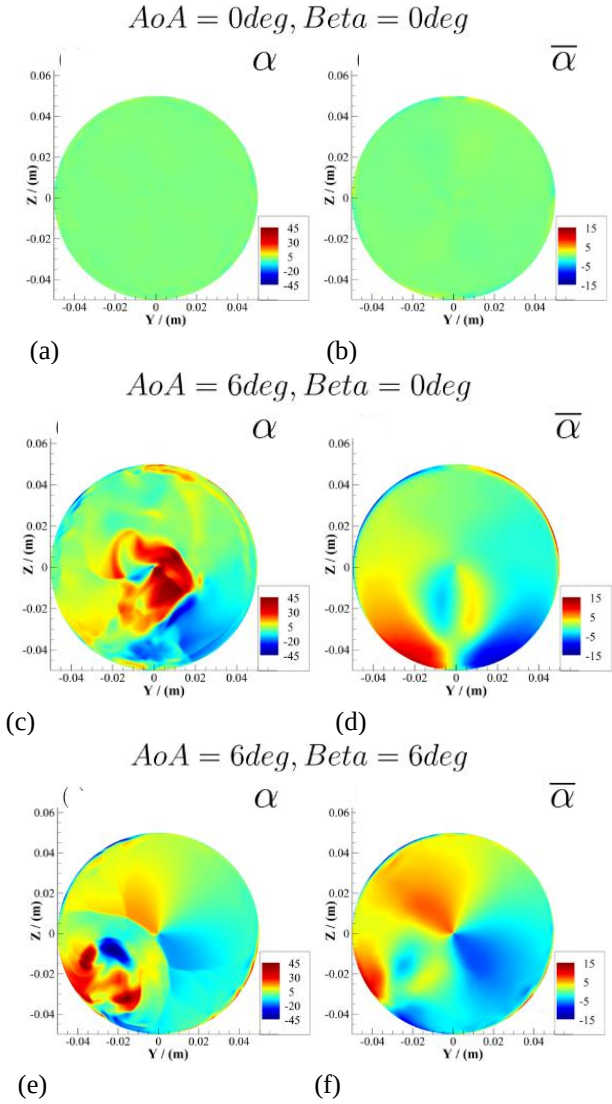

Fig. 13. Contours of instantaneous and time-averaged swirl angles at inlet exit plane.

seen that for the condition of Attack Angle = 0 deg, Sideslip Angle = 0 deg, both the transient and time-averaged swirl angles are small. This suggests that there is nearly no swirling flow under this condition. For the condition of Attack Angle = 6 deg, Sideslip Angle = 0 deg, as shown in Figs. 13(c) and 13(d), the region of positive swirl angle and the region of negative swirl angle are observed. According to the instantaneous contours, the region of positive swirl angle occupies the central portion of the exit plane of Busemann inlet, whereas the time-averaged contours reveal the presence of two pairs of positive and negative swirl angle regions near the bottom wall of exit plane of Busemann inlet. For the condition of Attack Angle = 6 deg, Sideslip Angle = 6 deg, as shown in Figs. 13(e) and 13(f), the swirl pairs are much larger than those for the condition of Attack Angle = 6 deg, Sideslip Angle = 0 deg, and the swirl pairs have an overall angle of inclination of 45 deg. These observations clearly show that for nonzero angles of attack and sideslip of the freestream, swirling flow will be generated in the Busemann inlet, and swirl pairs will appear at the exit plane of Busemann inlet.

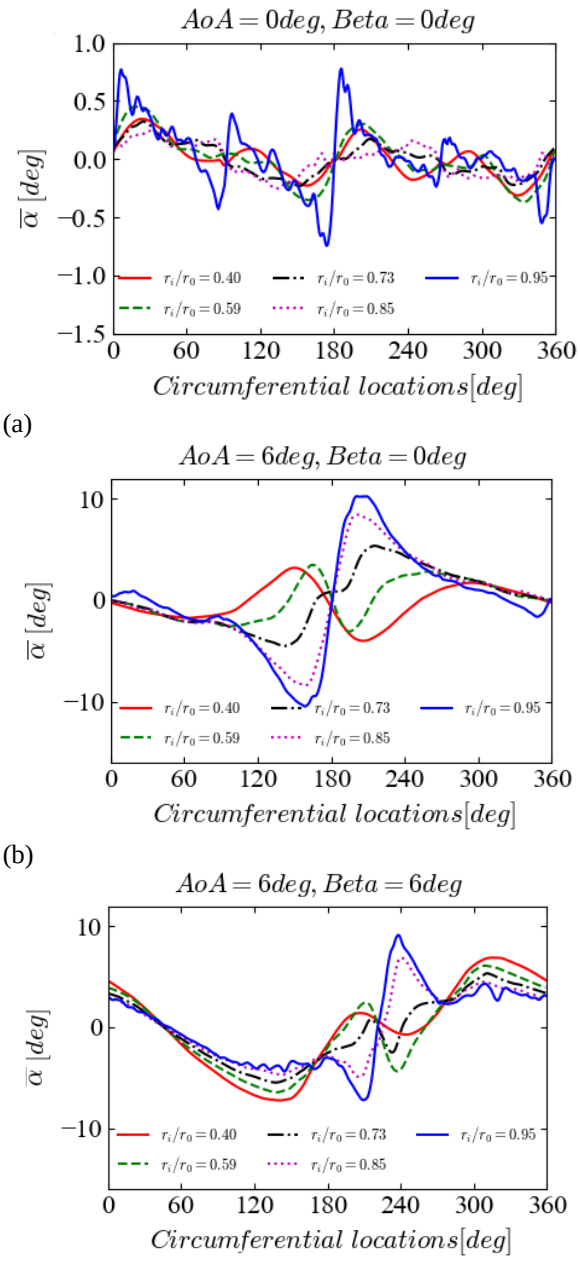

Fig. 14. Time-averaged total swirl angle distributions along the circumferential direction on five rings.

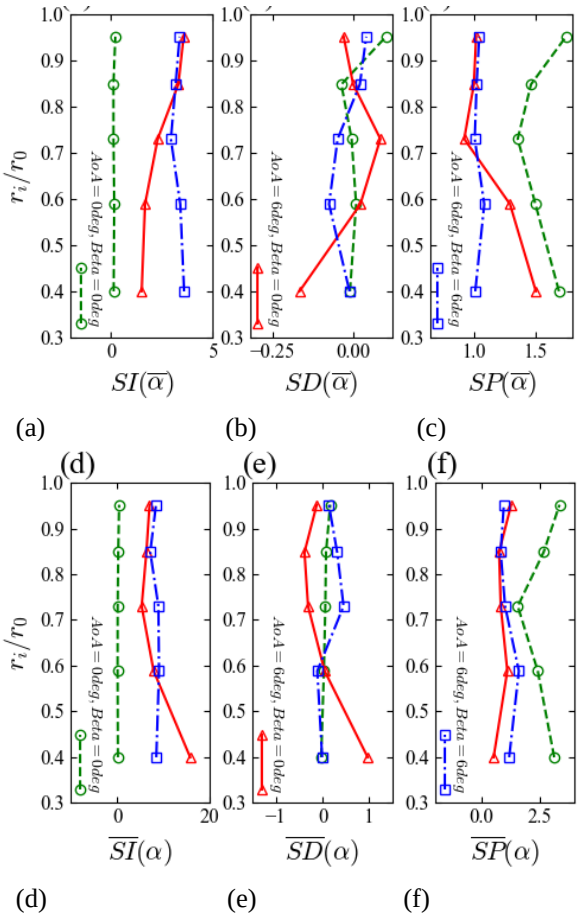

Fig. 15. Swirl distortion descriptors.

Figure 14 shows temporal-averaged swirl angle distributions along the circumferential direction on five rings. For the condition of Attack Angle = 0 deg, Sideslip Angle = 0 deg, as shown in Fig. 14(a), the swirl angles on all five rings are relatively small, ranging between −0.8 deg and 0.8 deg. The swirl angle on the outermost ring (r_i/r_0 = 0.95) undergoes obvious fluctuations, owing to the turbulent structures in the boundary layer. For the condition of Attack Angle = 6 deg, Sideslip Angle = 0 deg, as shown in Fig. 14(b), swirl pairs appear over the five rings, with the division between positive and negative swirl angles occurring at a circumferential location of 180 deg. The swirl angle distribution is consistent with what can be seen in Fig. 13(d). It can be seen that on the inner rings (r_i/r_0 = 0.40 and 0.50), the distribution of swirl angles is opposite to that on the outer rings (r_i/r_0 = 0.73, 0.85, and 0.95). This indicates that there are two swirl pairs at the inlet exit plane. For the condition of Attack Angle = 6 deg, Sideslip Angle = 6 deg, as shown in Fig. 14(c), similar swirl pairs are also observed, at circumferential locations between 180 deg and 275 deg, together with a larger swirl pair located between 60 deg and 180 deg and between 275 deg and 360 deg.

Figures 15(a)–15(c) and 15(d)–15(f) present swirl distortion descriptors calculated respectively from temporal-averaged swirl angle $\bar{\alpha}$ and from the average values based on the instantaneous swirl angle α. For the condition of Attack Angle = 0 deg, Sideslip Angle = 0 deg, the time-averaged swirl intensities (SD) are zero for all the rings. The swirl intensities for the two off-design conditions are much larger than those for the on-design condition, and in particular for the condition of Attack Angle = 6 deg, Sideslip Angle = 6 deg, the swirl intensities on the inner rings (r_i/r_0 = 0.40, 0.50, and 0.73) are much larger than those for the other two conditions. The results indicate that the combined effects of angle of attack as well as angle of sideslip of free steam will lead to greater swirl intensity. For the condition of Attack Angle = 6 deg, Sideslip Angle = 0 deg, the swirl directivities (SD) on the rings r_i/r_0 = 0.40 and r_i/r_0 = 0.73 are in the opposite directions. This is due to the two oppositely distributed swirl pairs at the inlet exit plane shown in Fig. 13(d). The average values of the fluctuating swirl distortion descriptors shown in Figs. 15(d)–15(f) are much larger than those calculated from the time-averaged swirl angle. This indicates that the swirl distribution in a Busemann inlet under off-design conditions exhibits significant

fluctuating features that greatly increase the level of swirl distortion.

5. CONCLUSIONS

In this study, large eddy simulations have been performed for a typical Busemann inlet at freestream Mach number 6 to explore the flow characteristics inside the inlet duct. The flow quantities at the exit plane of Busemann inlet have been used to evaluate the total pressure and swirl distortions. Both the on-design flow condition and two off-design conditions have been simulated to study the effects of freestream variations in angle of attack as well as angle of sideslip on Busemann inlet turbulent flow features as well as total pressure and swirl distortions.

It has been found that for the on-design flow condition (Attack Angle = 0 deg, Sideslip Angle = 0 deg), the shock structures and boundary layer development are axisymmetric about the inlet axis. The captured freestream is compressed smoothly through the inlet duct. The total pressure loss is primarily confined within the boundary layer region, and nearly no swirling flow appears during the inlet compression process. The fluctuating features of the Busemann inlet result mainly from turbulent boundary layer structures. Both total pressure distortion and swirl distortion are relatively small under the on-design flow condition.

Under the off-design flow conditions (Attack Angle = 6 deg, Sideslip Angle = 0 deg and Attack Angle = 6 deg, Sideslip Angle = 6 deg), the shock wave structures inside Busemann inlet duct become non-axisymmetric and lead to localized strong shock wave–boundary interactions. In the case of the off-design flow condition Attack Angle = 6 deg, Sideslip Angle = 0 deg, a large flow separation zone is observed owing to the incidence of a strong curved shock at the leeward side inside the inlet duct. The strong shock wave–boundary layer interaction also leads to evident total pressure losses when the separated flows pass the inlet exit plane. Meanwhile, large-scale swirling flow is formed owing to a nonuniform transverse pressure distribution along the circumferential direction at different axial sections from the inlet entrance plane to the exit plane. Under off-design conditions, swirl flow are found at the exit plane of Busemann inlet. The total pressure and swirl distortions for the Busemann inlet under off-design conditions are significantly larger than those under the on-design condition. The averages of the fluctuating distortions are evidently stronger than the temporal-averaged total pressure and swirl distortions. These results show that turbulent flow fluctuations are important in determining the overall distortion level in a Busemann inlet, and therefore particular attention should be paid to transient total pressure and swirl distortions when designing Busemann inlets and new types of hypersonic inlet based on the Busemann basic flow.

Acknowledgements

This research was funded by National Natural Science Foundation of China (Grant No. 12002144) and the Jiangxi Provincial Natural Science Foundation (Grant No.20212BAB211015).

CONFLICT OF INTEREST

The authors have no conflict of interest to disclose in this research work.

AUTHOR CONTRIBUTIONS

Yiqing Li: Oversight and leadership responsibility for the research activity planning and execution, including mentorship external to the core team. Zhenlong Wu: Part of the writing of the first draft, Data and information visualization, and revision of the returned draft. Shiqichang Wu: Writing of Part of the First Draft Songjian Hu: Construction of research models and grid partitioning. Feng Wei: Provide computing resources for this paper.

REFERENCES

AIR1419C (2017). Inlet total pressure distortion considerations for gas turbine engines. *SAE International*.

A*IR5686* (2017). A methodology for assessing inlet swirl distortion, *SAE International*.

ARP1420C (2017). Gas turbine engine inlet flow distortion guidelines. *SAE International*.

Bachchan, N., & Hillie, R. (2004a，August). Effects of Hypersonic Inlet Flow Non-Uniformities on Stabilising Isolator Shock Systems. *AIAA Atmospheric Flight Mechanics Conference and Exhibit*, Providence, Rhode Island.

Bachchan, N., & Hillie, R. (2004b, August). *Hypersonic inlet flow analysis at off-design conditions*. 22nd Applied Aerodynamics Conference and Exhibit, Providence, Rhode Island.

Brahmachary, S., & Ogawa, H. (2021). Multipoint design optimization of busemann-based intakes for scramjet-powered ascent flight. *Journal of Propulsion and Power*, 37:6, 850-867. https://doi.org/10.2514/1.B38383

Ding, F., Liu, J., Shen, C., & Huang, W. (2015). Novel inlet–airframe integration methodology for hypersonic waverider vehicles. *Acta Astronautica*, 111, 178-197. https://doi.org/10.1016/j.actaastro.2015.02.016

Ding, F., Liu, J., Shen, C., Huang, W., Liu, Z., & Chen, S. (2018). An overview of waverider design concept in airframe/inlet integration methodology for air-breathing hypersonic vehicles. *Acta Astronautica*, 152, 639-656. https://doi.org/10.1016/j.actaastro.2018.09.002

Flock, A. K., & Gülhan, A. (2016). Viscous effects and truncation effects in axisymmetric busemann scramjet intakes. *AIAA Journal*, 54:6, 1881-1891. https://doi.org/10.2514/1.J054287

Geurts, B. J., Kuerten, J. G. M., Vreman, A. W., Theofilis, V., & Zandbergen, P. J. (1993). A finite volume approach to compressible Large Eddy Simulations. *Applied Scientific Research*, 51, 325-329. https://doi.org/10.1007/978-94-011-1689-3_52

Heiser, W., Pratt, D., Daley, D., & Mehta, U. (1994). *Hypersonic airbreathing propulsion.* American Institute of Aeronautics and Astronautics, Reston, USA.

Luo, S., Sun, Y., Liu, J., Song J., & Cao, W., (2022). Performance analysis of the hypersonic vehicle with dorsal and ventral intake. *Aerospace Science and Technology*, 113 A, 1270-9638. https://doi.org/10.1016/j.ast.2022.107964

Ma, B., Wang, G., Wu, J., & Ye, Z. (2020). Avoiding choked flow and flow hysteresis of busemann biplane by stagger approach. *Journal of Aircraft*, 57(3), 440-455. https://doi.org/10.2514/1.C035664

Malo-Molina, F. J., Gaitonde, D. V., Ebrahimi, H. B., & Ruffin, S. M. (2010). Three-dimensional analysis of a supersonic combustor coupled to innovative inward-turning inlets. *AIAA Journal*, 48(3), 572-582. https://doi.org/10.2514/1.43646

McGann, B., Lee, T., Ombrello, T., Carter, C. D., Hammack, S. D., & Do, H. (2019). Inlet distortion effects on fuel distribution and ignition in scramjet cavity flameholder. *Journal of Propulsion and Power*, 35(3), 601-613. https://doi.org/10.2514/1.B37204

Mölder, S., & Szpiro, E. J. (1966). Busemann inlet for hypersonic speeds. *Journal of Spacecraft and Rockets*, 3(8), 1303-1304. https://arc.aiaa.org/doi/abs/10.2514/3.28649

Musa, O., Huang, G., & Yu, Z. (2022). Assessment of new pressure-corrected design method for hypersonic internal waverider intake. *Acta Astronautica*, 201, 230-246. https://doi.org/10.1016/j.actaastro.2022.09.001

Ombrello, T., Peltier, S., & Carter, C. D. (2015). *Effects of inlet distortion on cavity ignition in supersonic flow*. 53rd AIAA Aerospace Sciences Meeting, Kissimmee, Florida.

Ramunno, M. A., Boyd, I. M., Grandhi, R. V., & Camberos, J. (2022). Integrated hypersonic aeropropulsion model for multidisciplinary vehicle analysis and optimization. *Journal of Propulsion and Power*, 38(3), 478-488. https://doi.org/10.2514/1.B38573

Schulte, D., Henckels, A., & Neubacher, R. (2001). Manipulation of shock/boundary-layer interactions in hypersonic inlets. *Journal of Propulsion and Power*, 17(3), 585-590. https://doi.org/10.2514/2.5781

Wang, C., Tian, X., Yan, L., Xue, L., & Cheng, K. (2015). Preliminary integrated design of hypersonic vehicle configurations including inward-turning inlets. *Journal of Aerospace Engineering*, 28(6), 04014143. https://doi.org/10.1061/(ASCE)AS.1943-5525.0000480

Wang, X., Wang, J., & Lyu, Z. (2016). A new integration method based on the coupling of mutistage osculating cones waverider and Busemann inlet for hypersonic airbreathing vehicles. *Acta Astronautica*, 126, 424-438. https://doi.org/10.1016/j.actaastro.2016.06.022

Xie, W., Wu, Z., Yu, A., & Guo, S. (2018). Control of severe shock-wave/boundary-layer interactions in hypersonic inlets. *Journal of Propulsion and Power*, 34(3), 614-623. https://doi.org/10.2514/1.B36614

Xiong, B., Fan, X., & Wang, Y. (2019). Parameterization and optimization design of a hypersonic inward turning inlet. *Acta Astronautica*, 164, 130-141. https://doi.org/10.1016/j.actaastro.2019.07.004

Xu, S., Wang, Y., Wang, Z., Fan, X., & Xiong, B. (2022). Experimental investigations of hypersonic inlet unstart/restart process and hysteresis phenomenon caused by angle of attack. *Aerospace Science and Technology*, 126, 107621. https://doi.org/10.1016/j.ast.2022.107621

Yu, Z., Huang, G., & Xia, C. (2020). 3D inverse method of characteristics for hypersonic bump-inlet integration airbreathing vehicles. *Acta Astronautica*, 166, 11–22. https://doi.org/10.1016/j.actaastro.2019.09.015

Zhai, J., Zhang, C., Wang, F., & Zhang, W. (2022). Control of shock-wave/boundary-layer interaction using a backward-facing step. *Aerospace Science and Technology*, 126, 107665. https://doi.org/10.1016/j.ast.2022.107665

Zhang, Y., Tan, H., Zhuang, Y., & Wang, D. (2014). Influence of expansion waves on cowl shock/boundary layer interaction in hypersonic inlets. *Journal of Propulsion and Powe,r* 30(5), 1183-1191. https://doi.org/10.2514/1.B35090

Zhang, Y., Zhang, L., He, X., Deng, X., & Sun, H (2017). Detached eddy simulation of complex separation flows over a modern fighter 313 model at high angle of attack. *Communications in Computational Physics*, 22, 1309–1332. https://doi.org/10.4208/cicp.OA-2016-0132